ADVANCED OPTICAL MATERIALS
www.advopticalmat.de

Angle-Independent Top-Emitting Quantum-Dot Light-Emitting Diodes Using a Solution-Processed Subwavelength Scattering–Capping Layer

*Taesoo Lee, Minhyung Lee, Kyuho Kim, Hyunkoo Lee, Suk-Young Yoon, Heesun Yang, Sunkyu Yu, and Jeonghun Kwak**

Owing to the excellent optoelectronic properties of colloidal quantum dots (QDs), light-emitting diodes based on QDs (QLEDs) have been considered one of the most promising electroluminescence (EL) devices for full-color displays with a wide color gamut. Particularly, top-emission device architecture has been of interest to both academia and industry, because of the advantages in light outcoupling, aperture ratios, and integration with conventional backplanes. In this structure, however, angle-dependent color shifts originating from a variation in microcavity length are a critical issue that needs to be resolved. Here, a solution-processed dual-functional scattering–capping layer (SCPL) using ZnO nanoparticles on top-emitting QLEDs with ZnSeTe/ZnSe/ZnS QDs to modulate the optical interference is presented. By precisely controlling the thickness of the SCPL, the EL intensity and spectrum can be redistributed to produce a uniform color from any viewing angle. It is discovered that, unlike conventional CPLs, the formation of random nanocracks and nanoclusters in the SCPL adds subwavelength light-scattering capabilities, which promotes light extraction. The QLEDs with the solution-processed SCPL exhibit a 44% increase in the maximum external quantum efficiency, with completely imperceptible angle-dependent spectral shifts. The SCPL is expected to be applied to the development of high-performance and next-generation QLED displays.

1. Introduction

Colloidal quantum dots (QDs) are spotlighted as one of the most promising emitting materials for optoelectronic devices owing to their advantages, such as high photoluminescence (PL) quantum yield (QY),[1–3] narrow emission bandwidth,[4,5] and the capability of the solution process.[6,7] In addition to these outstanding properties of QDs, continuous efforts in device engineering have made QD-based light-emitting diodes (QLEDs) exhibit highly pure, efficient, and intense light emission.[8–12] For instance, the top-emission device architecture, which emits light through the top semi-transparent metal electrode, has been adopted to maximize the outcoupling efficiency of QLEDs by virtue of the microcavity effect between two reflective electrodes.[13–17] As a result, top-emission QLEDs generally show improved optoelectronic performance, such as higher luminance (L) and narrower full-width at half-maximum (FWHM) of the electroluminescence (EL) spectrum, which are required to achieve wide color gamut (WCG) displays. Moreover, top-emission QLEDs have benefits in their practical application to active-matrix display devices, because of the high aperture ratios and easy integration with conventional backplane technologies.[18] Despite these positive prospects, large color-shifts (i.e., changes in both light intensity and spectrum) depending on the viewing angle is one of the major challenges that need to be solved.[19,20]

To surmount the issue, in case of top-emission organic light-emitting diodes (OLEDs), a thin organic dielectric capping layer (CPL) has been often deposited by thermal evaporation over the

T. Lee, M. Lee, J. Kwak
Department of Electrical and Computer Engineering
Inter-university Semiconductor Research Center
and Soft Foundry Institute
Seoul National University
Seoul 08826, Republic of Korea
E-mail: jkwak@snu.ac.kr

The ORCID identification number(s) for the author(s) of this article can be found under https://doi.org/10.1002/adom.202302509

DOI: 10.1002/adom.202302509

K. Kim, S. Yu
Intelligent Wave Systems Laboratory
Department of Electrical and Computer Engineering
Seoul National University
Seoul 08826, Republic of Korea

H. Lee
Department of Electrical Engineering and Institute of Advanced Materials and Systems
Sookmyung Women's University
Seoul 04310, Republic of Korea

S.-Y. Yoon, H. Yang
Department of Materials Science and Engineering
Hongik University
Seoul 04066, Republic of Korea

semi-transparent top metal electrode.[21,22] The well-known effects and advantages of using a CPL are that it enables to modulate the optical interference in the cavity structure by tuning the CPL thickness.[23] When optimized, the light extraction to the normal direction can be enhanced and the FWHM can be narrowed down. Also, the angle-dependent color shift can be mitigated through optimization.[22] Nevertheless, there is a strong trade-off relationship between the device efficiency and the angular spectral shifts in top-emission devices, mainly due to the intense microcavity resonance.[19,20] In 2017, Tan et al. developed a multi-object algorithm that helps to precisely tune the optimal CPL conditions for lower spectral shifts, higher device efficiency, and wider color gamut,[24] resulting in broad application to top-emitting OLEDs. However, the effects of using the CPL in top-emitting QLEDs have rarely been investigated. A few researchers utilized a thermally-evaporated CPL on solution-processed QLEDs in the same way as that used in the top-emitting OLEDs, and reported improved light extraction.[18,19,25] Although thermal evaporation is a reasonable method to precisely control the CPL thickness, it is a costly process requiring a high vacuum chamber and fine metal shadow masks. For this reason, it is hard to deposit the CPLs in different thicknesses that are optimal for each of the red, green, and blue subpixels—even in commercial full-color OLEDs, only a single-thick CPL is formed to cover all the red, green, and blue pixels, which may be an optimum thickness only for a certain color. However, depending on the emission wavelength of top-emitting devices, the thickness of the CPL has a significant influence on their optical properties. Therefore, it is imperative to develop a novel CPL that can be finely tuned in its thickness with the solution-process compatibility in a simpler method.

Another way to enhance light extraction from light-emitting devices is to employ an additional light-scattering layer (SCL).[26–29] The SCL incorporates a microstructure, such as micro-lens arrays or random scattering (sub-)microparticles, to redirect light propagation and reduce total internal reflection (TIR) loss within the device.[20,30] However, fabrication of the SCL microstructure requires complicated microprocesses (e.g., photolithography, UV-exposure, and etching) which can damage the fabricated light-emitting devices. Also, consecutive deposition of the CPL and SCL adds complexity to the fabrication process. Above all, the thickness of the SCLs and the size of the constituents—ranging from hundreds of nanometers to several micrometers—is likely to increase haze and cause pixel crosstalk, hindering the practical use of SCLs. Moreover, these types of SCLs are unable to simultaneously function as CPLs because the scattering particles are usually on the wavelength scale. This size limitation makes it difficult to precisely tune the electromagnetic interferences which requires subwavelength thickness tuning to optimize the CPL. Therefore, as QLEDs are integrated into ultra-high-resolution displays with smaller pixels, especially for augmented reality (AR)/virtual reality (VR) displays which are emerging rapidly, thinner SCLs and smaller scattering particles are necessarily required to eliminate the aforementioned undesirable effects.

In this work, we introduce a novel dual-functional scattering–capping layer (SCPL) for the color-stable and efficient top-emitting QLEDs, comprised of a thin layer of ZnO nanoparticles (NPs), which is solution-processable and thickness tunable in a simple manner. To clearly verify the effects of the SCPL, we adopted the blue-emitting QLEDs with heavy metal-free ZnSeTe/ZnSe/ZnS QDs, and compared the device performance with the devices using a conventional CPL consisting of a thermal-evaporated organic layer. Interestingly, the top-emitting QLEDs with the SCPL exhibited superior light extraction properties compared to that with the conventional organic CPL under all experimental conditions, with up to 44% higher outcoupling efficiency than the device without a CPL. To reveal the origin of the superior optical properties of the SCPL, we performed an in-depth light-scattering simulation based on the meticulous investigation of the morphology of the ZnO thin-film, and found that it simultaneously functions as both the CPL and the SCL due to the naturally agglomerated ZnO NPs during the solution-based thin-film formation. More importantly, the QLEDs with the dual functional thin SCPL exhibit high color stability with nearly constant EL spectra across the entire viewing angle, while with no significant blurring that can cause pixel crosstalk. These features are becoming increasingly significant in forthcoming display devices due to the growing demand for higher resolution micro-display applications requiring complex optical designs, including AR/VR devices. In line with these requirements, our top-emitting QLED structure with the SCPL based on the subwavelength-scale agglomeration of ZnO NPs not only represents a promising strategy for achieving high optical properties, but also offers the possibility of fabricating fine-patterned SCPLs for each of the red, green, and blue subpixels in a simple solution-based process.

2. Results

2.1. Device Architecture and optimization

By closely observing the simulation results in Figure S1 (Supporting Information), the microcavity structure with blue-emitting QDs theoretically exhibited lower outcoupling efficiency than those with other visible colors (i.e., green–red) when the cavity lengths and the CPL thicknesses were individually optimized. This is practically unfavorable as it necessitates applying higher current densities (J) exclusively to blue-emitting pixels, which can accelerate their degradation compared to red/green pixels. Moreover, the blue color spectrum with a shorter wavelength (λ) is known to be more sensitive to the light scattering effect. Therefore, we focused on blue-emitting devices in this work to clearly observe the effects of the CPL/SCL, which is significantly important for reducing the efficiency gap between red/green and blue subpixels. A schematic device structure of the inverted top-emission QLED is illustrated in **Figure 1a**, which consists of Ag (100 nm, cathode)/ZnO NPs (25 nm)/[ZnSeTe/ZnSe/ZnS] QDs (15 nm)/9-(4-tert-butylphenyl)−3,6-bis(triphenylsilyl)−9H-carbazole (CzSi, 3 nm)/tris(4-carbazoyl-9-ylphenyl)amine (TCTA, 22 nm)/MoO_x (8 nm)/Ag (12 nm, anode). To compare the effects of the CPL on the QLED performance, we prepared the same structured devices with the conventional CPL and the SCPL of various thicknesses, and without a CPL. The cross-sectional transmission electron microscopy (TEM) images of the devices with the conventional CPL and the SCPL are shown in Figure 1b, along with the atomic force microscopy (AFM) images of the CPL surface. For the conventional CPL, we deposited 1,1-bis[(di-4-tolylamino)phenyl]cyclohexane (TAPC), an organic material

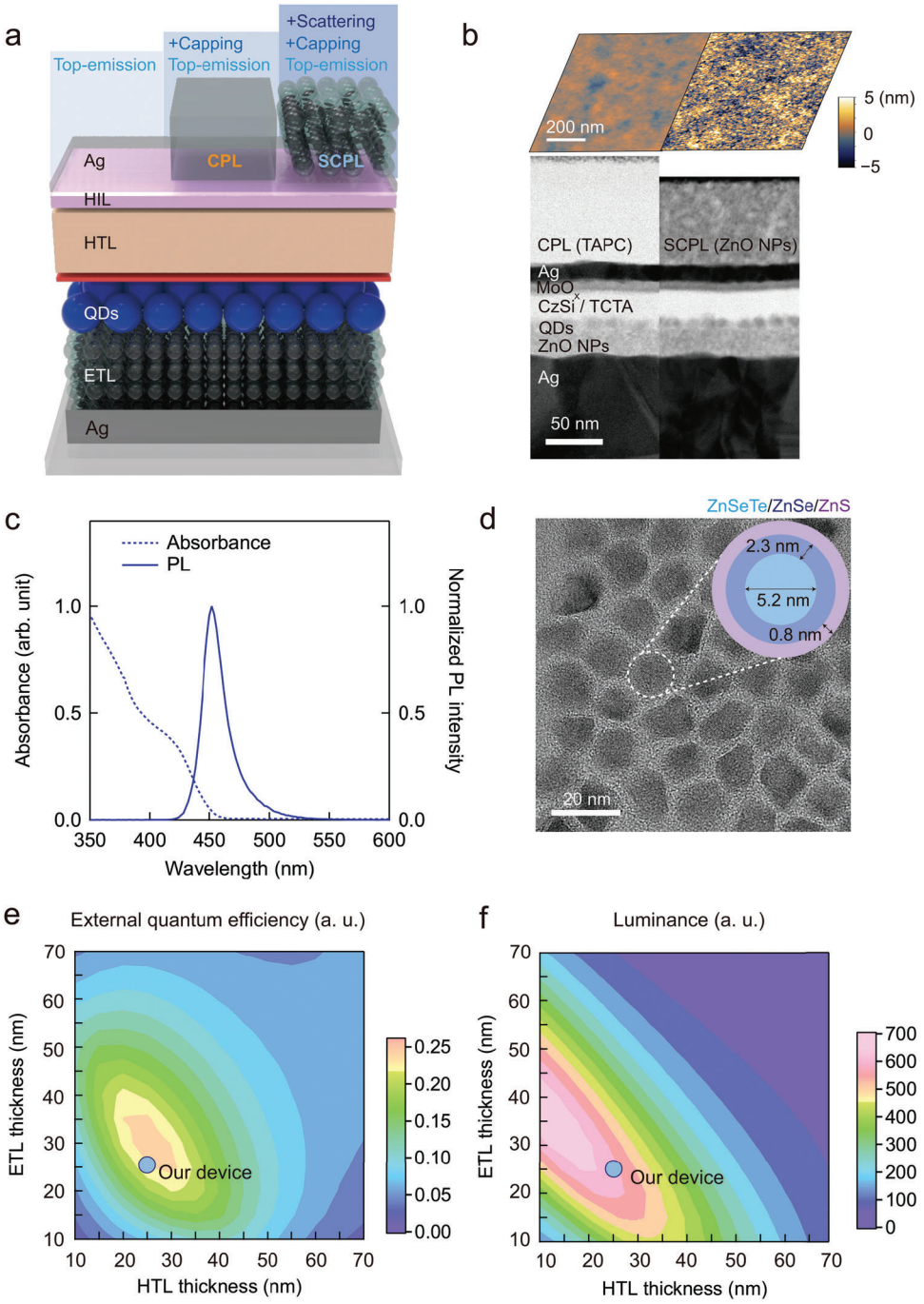

Figure 1. a) Schematic illustration of the top-emitting ZnSeTe/ZnSe/ZnS QLEDs without a CPL, with the conventional CPL and the SCPL. b) Cross-sectional TEM image of the top-emitting QLEDs with the conventional CPL (left) or the SCPL (right), and the AFM images showing their surface morphology. c) Absorbance and normalized PL spectrum of blue-emitting ZnSeTe/ZnSe/ZnS QDs, and d) their TEM image with dimensional information. e) Simulated EQE and f) *L* of the top-emitting blue QLEDs varying the thickness of the HTL and the ETL. Blue markers represent the experimental conditions of our devices.

having a refractive index (n) of 1.71 at $\lambda = 450$ nm, by thermal vacuum evaporation. For the SCPL, on the other hand, we deposited ZnO NPs by spin-coating, of which n is 1.64 at $\lambda = 450$ nm. Considering that n of the conventional CPL is slightly higher than that of the SCPL, the thicknesses of both CPLs were precisely adjusted to have a similar optical thickness (i.e., physical thickness divided by n). In addition, unlike the conventional CPL, the SCPL deposition requires the underlying layers of the QLED to be resistant to the deposition of ZnO NPs dispersed in 1-butanol. The cross-sectional TEM images show that both devices are almost identical in their initial thickness, indicating that the deposition of SCPLs causes no significant damage to the underlying layers.

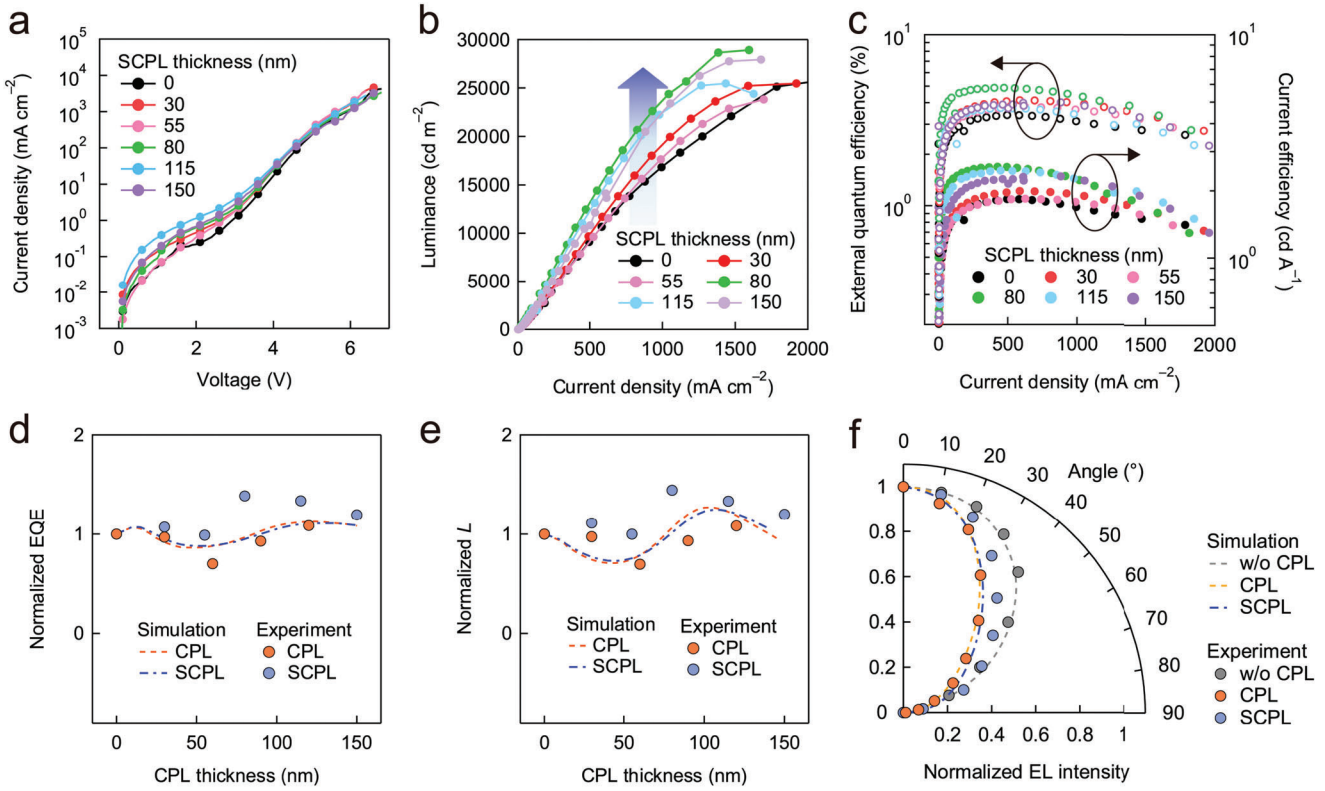

Figure 2. a) *J–V* and b) *L–J* characteristics, and c) the EQE and CE of the QLEDs with the SCPL thicknesses of 0, 30, 55, 80, 115, or 150 nm. d) Normalized EQE, and e) the normalized *L*, of the QLEDs with the organic CPL (orange) and the SCPL (blue). The dashed lines represent the simulated results and the markers indicate the experimental data measured when $J = 0.05$ A cm^{-2}. f) Simulated (dashed lines) and experimental (markers) angle-dependent EL intensity profiles of the QLEDs without a CPL (gray) and with the conventional CPL (orange) or the SCPL (blue).

Meanwhile, the AFM images comparatively show the morphological difference between the conventional CPL and the SCPL (Figure 1b; Figure S2, Supporting Information). In detail, the surface of the TAPC-based CPL presents a neat and highly uniform film morphology, whereas the ZnO NPs in the SCPL seem to agglomerate into larger clusters, which will be discussed later. For the emissive material, we employed heavy-metal-free, blue-emitting ZnSeTe/ZnSe/ZnS QDs with an average diameter of 11.4 nm, PL QY of 65%, peak wavelength (λ_{max}) at 452 nm, and a spectral FWHM of 23 nm. The absorption–emission spectra and a TEM image of the QDs are available in Figure 1c,d. Also, the TEM images of the QDs in each synthesis procedure are shown in Figure S3 (Supporting Information). The ZnO NPs and TCTA layers were adopted as the electron transport layer (ETL) and hole transport layer (HTL), respectively. The CzSi interlayer was inserted to optimize the charge balance, as we previously reported on its role.[14]

The distance between two reflective metal electrodes also plays a critical role in maximizing the light extraction. Before depositing the CPL or the SCPL, therefore, we optimized the first-order microcavity in our top-emission blue QLEDs by changing the HTL/ETL thickness based on optical simulations using a commercial optical simulation tool for thin-film devices (FLUXiM Setfos) to achieve superior performance in both EQE and *L*, as shown in Figure 1e,f. In our optimized device conditions (i.e., ETL 25 nm, HTL 25 nm), both factors reach 0.24 and 632 in arbitrary units, respectively, which are close to the theoretical maximum values (i.e., 0.26 for EQE and 697 for *L*). On this optimized device architecture, we finally deposited organic CPLs or ZnO NP-based SCPLs with different thicknesses, to study the effects and performance of the CPLs.

2.2. Performance of QLEDs with CPL

To investigate the effects of the CPLs, we first characterized the optoelectrical properties of the devices in detail by varying the thickness of the CPLs. In **Figure 2**a, the *J*–voltage (*V*) curves of the QLEDs with the SCPL are provided. Because the deposition of the SCPL hardly affects the underlying layers, the devices exhibit nearly identical *J–V* curves regardless of the SCPL thickness. Meanwhile, the *L* of the QLEDs with the SCPL was significantly improved, as shown in Figure 2b. When the SCPL thickness was 80 nm, the maximum *L* (L_{max}) increases to ≈29 000 cd m^{-2}, even though the EL spectrum changes from 457 to 455 nm, where human eye sensitivity decreases. The FWHM of the spectrum is narrowed down from 26.5 to 24.2 nm, as the SCPLs facilitate the microcavity effect due to the interference modulation (see **Table 1**; Figure S4, Supporting Information). Furthermore, the maximum EQE and current efficiency (CE) are also improved by ≈ 1.44-fold, from 3.4% to 4.9% and from 1.8 to 2.6 cd A^{-1}, respectively, as shown in Figure 2c and Table 1. Considering that

Table 1. Performance of the blue top-emitting QLEDs with various thicknesses of the SCPL.

SCPL thickness [nm]	EL λ_{max} [nm]	FWHM [nm]	Max. CE [cd A^{-1}]	EQE [%]	L at J = 1 A cm^{-2} [cd m^{-2}]	L_{max} [cd m^{-2}]
0	457	26.5	1.8	3.4	16 820	25 138
30	456	26.2	2.0	4.1	19 947	25 473
55	455	24.7	1.8	3.8	17 629	23 809
80	455	24.5	2.6	4.9	24 367	28 932
115	455	22.9	2.5	3.7	22 245	25 469
150	455	22.7	2.3	4.0	23 411	27 940

the EQE is expressed as the multiplication of the outcoupling efficiency and the internal quantum efficiency (IQE), it is noteworthy that these significant improvements are mainly attributed to the enhancement of the light outcoupling rather than the IQE, which can break the theoretical limit of the blue cavity structure (Figure S1c, Supporting Information). Table S1 (Supporting Information) provides an overview of diverse strategies employed to boost the performance of ZnSeTe-based QLEDs, offering additional insights that supplement the findings presented in this study. In the same way, we characterized the optoelectrical properties of the QLEDs with a conventional organic CPL. As shown in Figure S5 (Supporting Information), the L_{max}, EQE, and CE were fluctuated along with the CPL thickness due to the wave interference. The highest performance was obtained when the organic CPL thickness was 120 nm, where the L_{max} and CE were increased by ≈ 1.09 and 1.08-fold, respectively, compared with the device without a CPL. However, the enhancement was less than that of the devices with SCPLs, as summarized in Table S2 (the Supporting Information). As compared in Figure 2d–f, a large difference in optical performance (in terms of EQE, L, and angle-dependent EL intensity profiles) is observed between the devices with the SCPL and those with the conventional CPL. Although the refractive indices of the two CPLs are slightly different, such a large difference in light extraction properties was not intuitively understandable.

To unravel the cause of the above results, we performed optical simulations based on the effective medium theory (EMT) from which theoretical optical properties can be derived, and the results are plotted as dashed lines against the experimental results in Figure 2d–f. For more accurate simulations, the n and the extinction coefficient (k) of each layer are measured as a function of λ using an ellipsometer as the input parameters (Figure S6, Supporting Information). Since we first assumed that all the layers of the QLEDs including both types of the CPLs, are homogeneous media, the light-scattering effect was excluded at this stage. The experimental results of the devices without a CPL and with a conventional CPL showed a strong correlation with the EMT simulation results, demonstrating the reliability of the simulation for the devices with a TAPC-based CPL that were homogeneously deposited by thermal evaporation. On the contrary, the experimental performance of the SCPL devices was significantly higher than the EMT-based simulation results over the entire thickness range. This implies that there are additional factors other than the microcavity interference beyond the assumption of material homogeneity. Our speculation can be further supported by the fact that the angle-dependent EL spectra of the QLEDs with a SCPL are different from the simulated spectra, while those of the devices with a conventional CPL show a high similarity to the simulated data (see Figure S7, Supporting Information). This implies that the SCPL may additionally have a light-scattering ability. Therefore, verification considering the scattering effect of the SCPL was required.

2.3. Light-Scattering Effects of SCPL

Along with the cross-TEM and the AFM images shown in Figure 1b, we observed the morphologies of SCPLs using scanning electron microscopy (SEM) in **Figure 3**a, for all the thickness ranges (see Figure S8, Supporting Information). In the SEM images, we found that the SCPL film has a large number of random nanocracks with the size of ≈100 nm and nanoclusters, which originated from the agglomeration of ZnO NPs during the solution-based thin-film formation. According to the "multiple scattering theory" and the experimental results in Figure 2d–f, we speculate that the characteristic lengths of the ZnO NP nanoclusters and/or nanocracks exceed the limit of the first-order Born approximation which is the minimum size for the sub-wavelength light-scattering effect between densely distributed clusters/cracks.[31] This implies that multiple light-scattering should not be neglected in the QLEDs with SCPLs, and thus the SCPL should not be treated as a homogeneous medium as in the EMT simulation.

To elucidate the discrepancy between the theoretical predictions using the EMT and the empirical device performance, we performed a two-dimensional full-wave electromagnetic simulation for the scattering from the irregularly arranged ZnO nanoclusters with nanocracks. To reflect the actual morphologies of the SCPL, we modeled a simulation as illustrated in Figure 3b. In the simulation, the distribution of ZnO nanoclusters within the SCPL was defined by the distribution factor ρ, which represents the number of randomly arranged cluster centers at (x_c, y_c) with a diameter of 10 nm, allowing for the overlap of each cluster area. The diameter was determined from the cross-TEM image of the SCPL. The scattering effect of the conventional organic CPL was also calculated by considering it as a homogeneous layer in the same model. Details of this simulation modeling are described in the Experimental section and in Figure S9 (Supporting Information). This optical simulation presents that the 90-nm-thick organic CPL results in the reduced light intensity by the factor of ≈0.95, indicating no evidence of light scattering. Meanwhile, the light-scattering intensity of the 80-nm-thick SCPL varies along with ρ as plotted in Figure 3c, due to the change in the density of the ZnO nanoclusters and nanocracks. When ρ is 0.5, the light

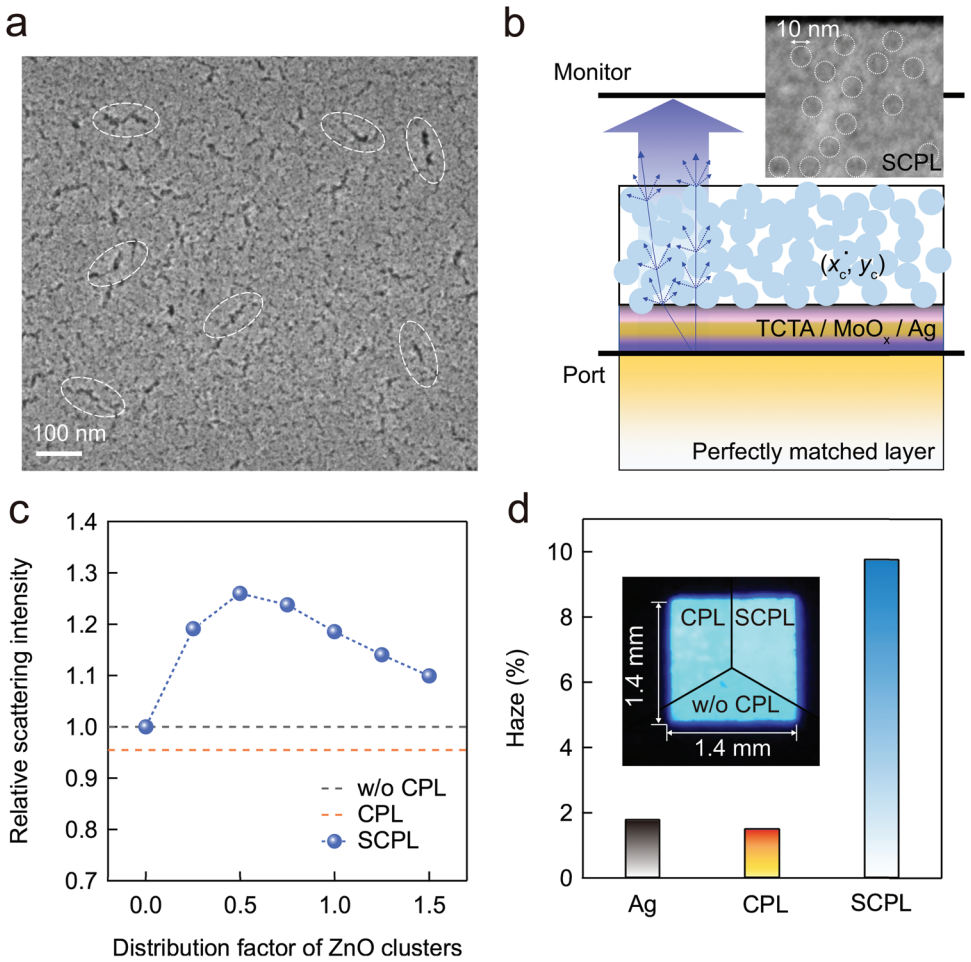

Figure 3. a) SEM image of the 80 nm-thick SCPL surface. A few of the naturally formed nanocracks are marked with dashed circles. b) Schematic illustration of the light-scattering simulation. The monochromatic waves (λ = 455 nm) were emitted from the port, passed through the randomly distributed ZnO nanocluster layer, and the light intensities were measured at the monitor. The cross-TEM image of the SCPL shows the diameter of each cluster. c) Relative scattering intensity of the QLEDs with the 80-nm-thick SCPL to the device without a CPL, as a function of ρ. Error bars are the standard deviations of the results from 20 realizations. The dashed lines are the scattering intensities of QLEDs without a CPL (gray) and with the conventional CPL (90 nm, orange). d) Haze of the Ag, Ag/conventional CPL, and Ag/SCPL films. The inset photograph compares the edges of each pixel.

scattering can be enhanced by ≈1.3 times, demonstrating the superior light-scattering property of the SCPL over the conventional organic CPL. The simulation results show that the nanoscale agglomeration of ZnO NPs and the resulting random nanocracks within the SCPL can induce additional light scattering, which can help explain the unexpected changes in the angular EL distribution and the EQE enhancement. Our simulation modeling also implies that the material candidates for the SCPL are not limited to ZnO NPs, but can be expanded to various NPs, such as TiO_2, SiO_2, and NiO, if these kinds of NPs have appropriate properties (e.g., transparency, refractive index, and size-tunability) and aggregate into subwavelength-scale nanoclusters in film. Comprehensively, the main mechanisms by which the SCPLs can enhance the optical properties of QLEDs can be summarized as twofold. First, by controlling the thickness of the SCPL, the optical interference can be optimized, and the angular EL spectra and intensity can be redistributed. Second, the naturally formed subwavelength-scale ZnO clusters and nanocracks in the SCPL can induce multiple light scattering to further enhance the light extraction. In addition, slightly higher haze of the SCPL compared to that of conventional CPLs, as shown in Figure 3d, can scatter light more in lateral directions, which clearly explains the broadened angular distribution of EL spectra in Figure 2f. It should be noted that higher haze is not necessarily desirable as it can cause blurring problems, but the inset in Figure 3d obviously shows that our SCPL has clear pixel edges and almost no blurring due to its thinness.

2.4. Angle-Dependent Emission Characteristics in QLEDs

In the case of top-emission QLEDs, it is a concern that the EL spectrum differs depending on the viewing angle as the cavity length varies. When the devices are tilted, the EL emission tends to be slightly blue-shifted,[32] which is a major hurdle for top-emitting QLEDs to present a uniform color. To solve this

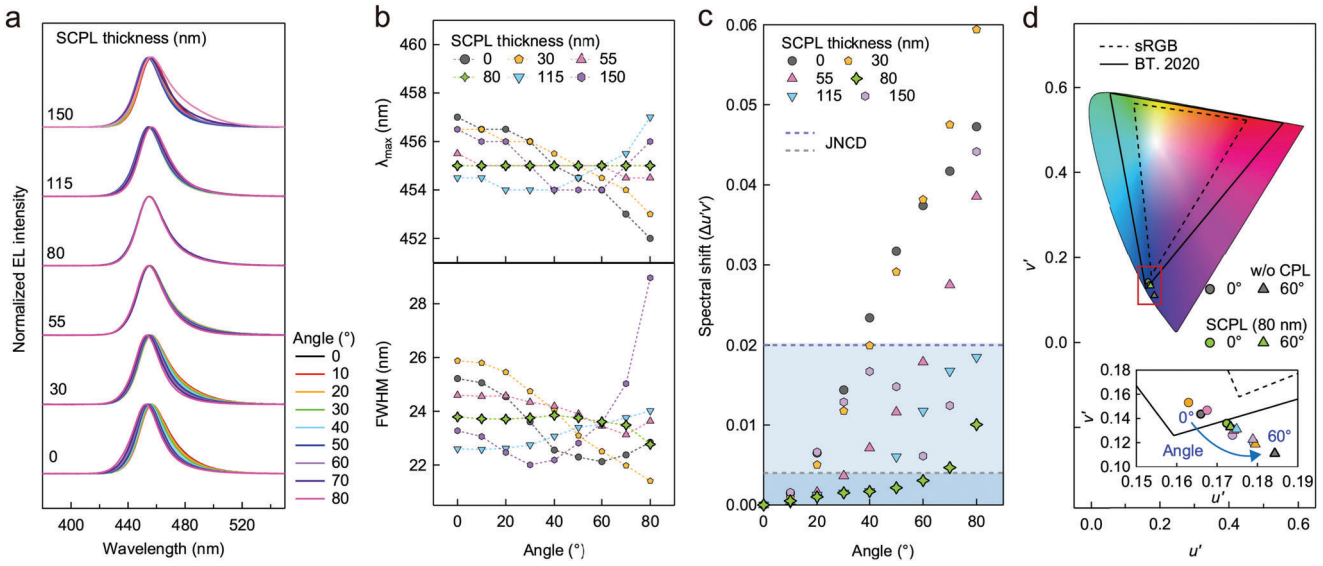

Figure 4. a) Angle-dependent EL spectra of QLEDs when the thickness of the SCPL was varied to 0, 30, 55, 80, 115, or 150 nm. During the measurement, the viewing angle was gradually tilted from 0° to 80° with an interval of 10°. b) Changes in λ_{max} (top) and FWHM (bottom), and c) the changes in CIE 1976 coordinates of the EL spectrum ($\Delta u''v''$) as a function of the viewing angle. The reference point of $\Delta u''v''$ was set when the viewing angle was 0°. The dashed lines represent the JNCD. d) CIE 1976 coordinates (u', v') of the EL spectrum of the QLEDs without a CPL (gray markers), with the 80-nm-thick SCPL (green markers), and with the other thickness of SCPLs (inset), along with the sRGB (dashed lines) and BT.2020 (solid lines) color spaces. The measurement angles for the EL spectrum are 0° for circle markers and 60° for triangle markers.

problem, it has been reported that the angle-dependent color shift can be mitigated by incorporating an appropriate thickness of a CPL to modulate the Fabry-Perot resonance factor.[33] However, previous CPLs had limitations due to the vacuum evaporation process of the CPLs, that is, the material availability is mostly limited to the small molecules, and controlling the thickness based on the emitting color adds complexity to the process steps. An additional SCL has been used to mitigate angular color shifts,[20,26] but the micron-scale scattering materials are highly likely to cause pixel crosstalk in a high-resolution pixel array. Moreover, stacking solution-processed SCLs on top of organic CPLs further complicates processability.

With the introduction of the SCPL, we could completely eliminate the angular shifts of the EL emission, while perfectly addressing the limitations of the previous studies owing to the dual-functionality of CPLs and SCLs. **Figure** 4a shows the EL spectra of the QLEDs with various thicknesses of the SCPL when the viewing angle is changed from 0° to 80°, of which the peak wavelength and FWHM are plotted in Figure 4b. The EL spectra of the QLED without a CPL exhibit blue-shifts in λ_{max} with increasing viewing angle. On the contrary, as the SCPL is covered, the shift of λ_{max} gradually decreases and almost disappears when the SCPL thickness is 80 nm, and increased again thereafter. Moreover, the changes in the FWHM of the devices also exhibited a similar behavior, which was minimized at the SCPL thickness of 80 nm. To quantify the degree of color shifts, we calculated the changes in the Commission internationale de l'éclairage (CIE) 1976 color coordinates ($\Delta u'v'$) as the viewing angle was tilted from 0° to 80° (see Figure 4c), which is defined as,[34,35]

$$\Delta u'v'(\theta) = \sqrt{\left(u'_\theta - u'_0\right)^2 + \left(v'_\theta - v'_0\right)^2} \quad (1)$$

where (u'_θ, v'_θ) is the color coordinate of the emission spectrum measured at a viewing angle θ, and (u'_0, v'_0) is the reference point, where θ is 0°. When evaluating color reproducibility, there is a standard that is mainly used in the display industry—just noticeable color difference (JNCD).[32] This means that the human eye can perceive the color difference of adjacent pixels when $\Delta u'v' = 0.004$. Thus, when $\Delta u'v'$ becomes larger than 0.004, a color change can be detected in a situation where one needs to see pixels from various angles simultaneously, such as flexible, foldable, or AR/VR displays. Additionally, the color difference in different spaces or timestamps can be noticed when $\Delta u'v' = 0.02$. As plotted in Figure 4c, $\Delta u'v'$ of the QLED without a CPL exceeds the JNCD (i.e., 0.02) from the viewing angle of 40°, and reaches almost 0.05 at 80° which is far beyond the human perception limit. However, when the 80-nm-thick SCPL is introduced, $\Delta u'v'$ is below 0.004 even up to the viewing angle of 60°, and it is still below 0.02 at 80°. This means that the angle-dependent color shift becomes unrecognizable with the SCPLs, which is highly advantageous for our top-emitting QLEDs to be applicable to a wide range of displays with various form factors. Furthermore, the device with the 80-nm-thick SCPL can contribute to covering a wide color gamut with imperceptible color shifts, as shown by the changes marked in Figure 4d compared to the sRGB and the BT.2020 color spaces.[36] On the other hand, it can be seen that the QD device without a CPL deviates significantly from the blue color coordinate of BT.2020 as the viewing angle increases. Figure S10 (Supporting Information) shows that adopting an appropriate thickness of the conventional CPL can also reduce the angle-dependent color shifts; however, the optimal device still exhibits $\Delta u'v'$ higher than the JNCD at the viewing angle of 80°, which means that the optical performance of the SCPL surpasses that of the conventional organic CPL. Therefore, we

believe that the introduction of the new SCPL would contribute to the development of color-stable WCG display devices based on top-emitting structured light-emitting diodes, including QLEDs, OLEDs, and perovskite LEDs, in a simple solution process.

3. Conclusion and Discussion

In this work, we demonstrate viewing angle-independent, top-emitting blue QLEDs with enhanced light outcoupling properties by introducing a solution-processed, dual-functional SCPL using subwavelength-scale ZnO NPs. Compared with conventional CPLs, our SCPL exhibits much higher optical performance in both color shifts and light scattering, which is attributed to the naturally formed ZnO nanoclusters and random nanocracks. We think that the introduction of the SCPL is even more promising in practice because of the following advantages. First, the SCPL based on solution-processed ZnO NPs performs the functions of both CPLs and SCLs simultaneously, reducing fabrication steps and costs. Second, solution-based patterning enables SCPL thickness to be optimized separately for each primary color, as shown in Figure S1 (Supporting Information). While the SCPL in this study was spin-coated on QLEDs to form non-pixelated blue devices, the final stage of commercialization will involve a patterning method, and the optimization for each color can be different. Unlike the conventional CPLs, which require complicated vacuum thermal evaporation processes and three different fine metal masks for each color, SCPLs can be more easily patterned by various solution processes, such as inkjet printing and transfer printing methods. By using various SCPL materials, more sophisticated optimizations for individual subpixels can be conducted, including the thickness control for cavity tuning and nanoparticle size control for scattering optimization. Finally, the use of a thin film (≈100 nm) from the extremely small-sized nanoparticles (≈3 nm) overcome most of the adverse effects that can be seen in high-resolution display arrays with small subpixels. Therefore, we strongly believe that the SCPL based on ZnO NPs would be a promising novel type of CPL for a wide range of top-emitting LEDs, such as polymer LEDs, perovskite LEDs as well as QLEDs, to enhance their optical properties. Furthermore, the subwavelength tunability of NP clustering with nanocracks would provide promising insights not only to the community for the development of color-stable and efficient display products, but also to the field of metamaterials and disordered photonics, such as the design of isotropic effective material parameters.

4. Experimental Section

Materials: Zinc acetate dihydrate ($Zn(CH_3CO_2)_2{\bullet}2H_2O$, ≥ 98%), potassium hydroxide (KOH, reagent grade, 90%), butylamine (99.5%), sulfur (99.998%, metal basis), tellurium (99.8%, powder), oleic acid (OA, 90%), 1-octadecene (ODE, 90%), trioctylamine (TOA, 98%), and 1-hexadecylamine (HAD, 98%) were purchased from Sigma–Aldrich. Zinc acetate ($Zn(CH_3CO_2)_2$, ≥ 99.9%) and selenium (99.999%, powder) were purchased from Alfa Aesar. Diphenylphosphine (DPP, > 98%) and trioctylphosphine (TOP, ≥ 99%) were obtained from Lake Materials.

Synthesis of ZnO NPs: In a three-necked round-bottomed flask, 2.0 g of $Zn(CH_3CO_2)_2{\bullet}2H_2O$ and 80 mL of methanol were mixed for reaction under N_2 condition at 60 °C. While stirring, 0.93 g of KOH dissolved in methanol (40 mL) was quickly injected into the $Zn(CH_3CO_2)_2{\bullet}2H_2O$ solution. After reacting for 145 min, the synthesized ZnO NPs were stabilized overnight. Finally, the product was precipitated, centrifuged with methanol for purification, and redispersed in 1-butanol with addition of butylamine (1 vol%) for stabilization.

Synthesis of Blue ZnSeTe/ZnSe/ZnS QDs: For the synthesis of the ZnSeTe QD core, 2 mmol of $Zn(CH_3CO_2)_2$ was placed in a three-necked flask with 2 mL OA and 20 mL of ODE. The cation mixture was degassed by heating to 120°C for 30 min and then it was heated to 210°C under N_2 purge. Then, a Se-DPP stock solution (1.0 mmol of Se dissolved in 0.5 mL of DPP) and a Te-TOP stock solution (0.029 mmol of Te dissolved in 0.6 mL of TOP) were co-injected into the mixture. For the growth of ZnSeTe cores, the reaction was maintained at 210°C for 30 min, followed by the reaction at 300°C for 1 h. For the formation of the ZnSe inner shell, a $Zn(OA)_2$ stock solution (15 mmol of $Zn(CH_3CO_2)_2$ dissolved in 10 mL of OA, 5 mL of TOA and 5 mL of TOP) and a Se stock solution (6 mmol of Se dissolved in 5 mL of TOP) were slowly added at a rate of 25 mL min^{-1} for 1 h, and the reaction was maintained at 300°C for 1 h. The reactor was then cooled down to room temperature, and the resulting ZnSeTe/ZnSe QDs were precipitated with ethanol and redispersed in 6 mL of hexane. Subsequently, to grow the ZnS outer shell, 6 mmol of $Zn(CH_3CO_2)_2$, 12 mmol of HAD, 6 mL of OA, and 60 mL of TOA were mixed in a three-necked flask with degassing at 120°C for 30 min. The 6 mL of the purified ZnSeTe/ZnSe QDs in hexane were injected into the reactor and degassed at 150°C for 10 min. After heating the reactor to 330°C under N_2 atmosphere, 18 mL of the $Zn(OA)_2$ stock solution and a S stock solution (5.6 mmol of S dissolved in 4.5 mL of TOP) were slowly added at a rate of 22.5 mL min^{-1} for 1 h and the reaction was maintained at 330°C for 1 h. As-synthesized ZnSeTe/ZnSe/ZnS QDs were repeatedly purified with hexane–ethanol-mixed solvent by centrifugation (9000 rpm, 10 min), and redispersed in hexane.

Device Fabrication: Glass substrates were ultrasonically cleaned with acetone, isopropyl alcohol, and deionized water for 15 min each. After drying in an oven at 120°C overnight, Ag was deposited by thermal evaporation through the cathode-patterned metal mask. Then, ZnO NPs (13 mg mL^{-1} dissolved in 1-butanol) were spin-coated at 2000 rpm for 40 s and annealed at 100°C for 30 min in an N_2-filled oven. After that, the ZnSeTe/ZnSe/ZnS QDs (4 mg mL^{-1} dissolved in hexane) were deposited by spin-coating at 4000 rpm for 30 s, and annealed at 60°C for 10 min in an Ar atmosphere. On the QD film, CzSi, TCTA, MoO_x, and Ag were thermally evaporated to form the hole transport layer, hole injection layer, and anodes, respectively. After fabricating the top-emitting QLEDs, various thicknesses of CPLs were deposited either by spin-coating the ZnO NPs or by thermal evaporation of TAPC. The ZnO NPs (15, 30, 45, 60, or 75 mg mL^{-1} dissolved in 1-butanol) were spin-coated at 2000 rpm for 40 s in an Ar-filled glove box to form SCPL, while TAPC was thermally evaporated to form the conventional CPL.

Characterization: The *J*–*V*–*L* characteristics of the QLEDs were measured using a Keithley 236 source–measurement unit, a Keithley 2000 multimeter, and a calibrated Si photodiode (Hamamatsu S5227-1010BQ). The EL spectra were measured using a spectroradiometer (Konica–Minolta CS-2000). The angle-dependent EL intensities and spectra were also measured using the spectroradiometer, while the samples were gradually rotated. The surface morphology was measured by AFM (Park Systems NX-10) and SEM (ZEISS GeminiSEM 560), and the cross-sectional image of the QLEDs was obtained by a high-resolution scanning transmission electron microscope (STEM, JEOL JEM-ARM200F). To obtain the input parameters for the optical simulation, the *n* and *k* of each layer were measured using an ellipsometer (Ellipsotechnology Elli-SE-UaM8). The absorption and PL emission spectra of the QDs were obtained using a UV/Vis spectrometer (Cary 5000, Varian) and a fluorescence spectrophotometer (F-2500, Hitachi), respectively. The haze of the CPL was obtained using a hazemeter (Nippon Denshoku NDH-2000) equipped with a D65 standard light source.

Simulation Methods: To simulate the wave interference throughout the CPL, a commercial thin-film device optical simulation tool, Setfos (FLUXiM, Switzerland), was used. All the consisting layers of the QLEDs, including the SCPL, were considered homogeneous in the simulation.

To simulate the light-scattering effect of the SCPL, two-dimensional finite element modeling was performed using COMSOL Multiphysics, as shown in Figure S9 (Supporting Information). The simulated structure was TCTA (perfectly matched layer)/light-emitting port (white line)/TCTA (25 nm)/MoO_x (8 nm)/Ag (12 nm)/SCPL (80 nm)/air/air (perfectly matched layer) (Figure S9a, Supporting Information). At the port, the monochromatic waves (λ = 455 nm) were randomly emitted at each viewing angle while monitoring the light intensity in air. The n of the SCPL was measured to be 1.64 by an ellipsometer at λ = 455 nm. However, the n of the single ZnO NP is expected to be higher considering that the SCPL possesses numerous air gaps inside the layer. The n of the single ZnO NP was assumed to be the same as that of a crystalline ZnO film, which was previously reported to be n = 2.1 at the wavelength of 450 nm.[37] Moreover, considering that ZnO clusters are composed of closely-packed ZnO NPs with a few air gaps, n of each cluster was set to be 1.8. To realize the inhomogeneous morphology of the SCPL, the film was modeled as follows (see Figure S9b, Supporting Information). The density of ZnO NP clusters within the SCPL was defined by the distribution factor $\rho = N(A_{ZnO}/A_{SCPL})$, where A_{ZnO} and A_{SCPL} are the areas of a cluster and the entire SCPL, respectively, and N is the number of ZnO NP clusters determined by ρ. The position of the cluster center (x_c, y_c) was determined by the uniform random distribution, allowing for their overlap. The radius of the ZnO NP clusters was set to be 5 nm based on the cross-TEM image of SCPL, which was reasonably consistent with the study in which the hydrodynamic diameter of aggregated ZnO NPs dissolved in 1-butanol was measured to be ≈ 10 nm.[38] Despite their overlap, n of the entire areas filled with ZnO clusters was assumed to be 1.8. The scattering efficiency was averaged over 20 random realizations to provide an ensemble average of the realizations, as illustrated in Figure S9c (Supporting Information). The scattering effect of the conventional CPL based on the identical model, consisting of TCTA (perfectly matched layer)/light-emitting port (white line)/TCTA (25 nm)/MoO_x (8 nm)/Ag (12 nm)/organic CPL (TAPC, 90 nm)/air/air (perfectly matched layer) was simulated. The conventional CPL was considered as a homogeneous layer with the n of 1.71.

Supporting Information

Supporting Information is available from the Wiley Online Library or from the author.

Acknowledgements

This work was supported by the Technology Innovation Program (20010737 and 20016332) funded by the Ministry of Trade, Industry & Energy (MOTIE, Korea) and by the National Research Foundation of Korea (NRF) grants (2021R1A4A3032027 and 2022R1A4A1028702) funded by the Ministry of Science and ICT (MSIT, Korea).

Conflict of Interest

The authors declare no conflict of interest.

Data Availability Statement

The data that support the findings of this study are available from the corresponding author upon reasonable request.

Keywords

angle-independent, quantum-dot light-emitting diodes, subwavelength scattering, top-emission

Received: October 5, 2023
Revised: December 20, 2023
Published online:

[1] X. Peng, L. Manna, W. Yang, J. Wickham, E. Scher, A. Kadavanich, A. P. Alivisatos, *Nature* **2000**, *404*, 59.
[2] J. Kwak, W. K. Bae, D. Lee, I. Park, J. Lim, M. Park, H. Cho, H. Woo, D. Y. Yoon, K. Char, S. Lee, C. Lee, *Nano Lett.* **2012**, *12*, 2362.
[3] D. A. Hanifi, N. D. Bronstein, B. A. Koscher, Z. Nett, J. K. Swabeck, K. Takano, A. M. Schwartzberg, L. Maserati, K. Vandewal, Y. van de Burgt, A. Salleo, A. P. Alivisatos, *Science* **2019**, *363*, 1199.
[4] P. Ramasamy, N. Kim, Y.-S. Kang, O. Ramirez, J.-S. Lee, *Chem. Mater.* **2017**, *29*, 6893.
[5] E.-P. Jang, C.-Y. Han, S.-W. Lim, J.-H. Jo, D.-Y. Jo, S.-H. Lee, S.-Y. Yoon, H. Yang, *ACS Appl. Mater. Interfaces* **2019**, *11*, 26062.
[6] H. Roh, D. Ko, D. Y. Shin, J. H. Chang, D. Hahm, W. K. Bae, C. Lee, J. Y. Kim, J. Kwak, *Adv. Opt. Mater.* **2021**, *9*, 2002129.
[7] M. K. Choi, J. Yang, K. Kang, D. C. Kim, C. Choi, C. Park, S. J. Kim, S. I. Chae, T.-H. Kim, J. H. Kim, T. Hyeon, D.-H. Kim, *Nat. Commun.* **2015**, *6*, 7149.
[8] T. Lee, B. J. Kim, H. Lee, D. Hahm, W. K. Bae, J. Lim, J. Kwak, *Adv. Mater.* **2022**, *34*, 2106276.
[9] Y. Sun, Q. Su, H. Zhang, F. Wang, S. Zhang, S. Chen, *ACS Nano* **2019**, *13*, 11433.
[10] Y.-H. Won, O. Cho, T. Kim, D.-Y. Chung, T. Kim, H. Chung, H. Jang, J. Lee, D. Kim, E. Jang, *Nature* **2019**, *575*, 634.
[11] T. Kim, K.-H. Kim, S. Kim, S.-M. Choi, H. Jang, H.-K. Seo, H. Lee, D.-Y. Chung, E. Jang, *Nature* **2020**, *586*, 385.
[12] H. J. Jang, J. Y. Lee, G. W. Baek, J. Kwak, J.-H. Park, *J. Inf. Disp.* **2022**, *23*, 1.
[13] L. H. Smith, J. A. E. Wasey, W. L. Barnes, *Appl. Phys. Lett.* **2004**, *84*, 2986.
[14] T. Lee, D. Hahm, K. Kim, W. K. Bae, C. Lee, J. Kwak, *Small* **2019**, *15*, 1905162.
[15] J. Kim, A. Hong, D. Hahm, H. Lee, W. K. Bae, T. Lee, J. Kwak, *Adv. Opt. Mater.* **2023**, *11*, 2300088.
[16] D. Li, J. Feng, Y. Zhu, Z. Lu, C. Pei, Z. Chen, Y. Li, X. Li, X. Xu, *Nano Res.* **2021**, *14*, 4243.
[17] X. Yang, E. Mutlugun, C. Dang, K. Dev, Y. Gao, S. T. Tan, X. W. Sun, H. V. Demir, *ACS Nano* **2014**, *8*, 8224.
[18] K.-Y. Lai, S. Yang, T.-C. Tsai, I.-A. Yao, C.-L. Yang, C.-C. Chang, H.-S. Chen, *Nanomaterials* **2022**, *12*, 2683.
[19] G. Liu, X. Zhou, S. Chen, *ACS Appl. Mater. Interfaces* **2016**, *8*, 16768.
[20] L. Shi, S. Chen, *ACS Appl. Mater. Interfaces* **2022**, *14*, 30039.
[21] J. W. Huh, J. Moon, J. W. Lee, D.-H. Cho, J.-W. Shin, J.-H. Han, J. Hwang, C. W. Joo, H. Y. Chu, J.-I. Lee, *Org. Electron.* **2012**, *13*, 1386.
[22] B. Hu, H. Chen, C. Li, W. Huang, M. Ichikawa, *Appl. Opt.* **2020**, *59*, 4114.
[23] Q. Huang, K. Walzer, M. Pfeiffer, K. Leo, *J. Appl. Phys.* **2006**, *100*, 064507.
[24] G. Tan, J.-H. Lee, S.-C. Lin, R. Zhu, S.-H. Choi, S.-T. Wu, *Opt. Express* **2017**, *25*, 33629.
[25] H. Wang, Y. Zhang, Y. Liu, Z. Chen, Y. Li, X. Li, X. Xu, *Nanoscale Adv.* **2023**, *5*, 1183.
[26] K. Ding, Y. Fang, S. Dong, H. Chen, B. Luo, K. Jiang, H. Gu, L. Fan, S. Liu, B. Hu, L. Wang, *Adv. Opt. Mater.* **2018**, *6*, 1800347.
[27] J. H. Kwack, J. Choi, C. H. Park, H. Hwang, Y. W. Park, B.-K. Ju, *Sci. Rep.* **2018**, *8*, 14311.
[28] K. An, C. Kim, S. Kim, T. Lee, D. Shin, J. Lim, D. Hahm, W. K. Bae, J. Y. Kim, J. Kwak, J. Kim, K.-T. Kang, *Small* **2023**, *19*, 2206133.
[29] C. Yuan, F. Tian, S. Chen, *Nano Res.* **2023**, *16*, 5517.
[30] J.-W. Kim, J.-H. Jang, M.-C. Oh, J.-W. Shin, D.-H. Cho, J.-H. Moon, J.-I. Lee, *Opt. Express* **2014**, *22*, 498.
[31] A. Gonis, W. H. Butler, *Multiple Scattering in Solids*, Springer Science & Business Media, Berlin, Germany **1999**.

[32] C. Dong, X. Fu, S. Amoah, A. Rozelle, D.-H. Shin, A. Salehi, J. Mendes, F. So, *J. Inf. Disp.* **2019**, *27*, 469.
[33] E. Kim, J. Chung, J. Lee, H. Cho, N. S. Cho, S. Yoo, *Org. Electron.* **2017**, *48*, 348.
[34] A. R. Robertson, *Color Res. Appl.* **1977**, *2*, 7.
[35] R. Lu, Q. Hong, Z. Ge, S.-T. Wu, *Opt. Express* **2006**, *14*, 6243.
[36] R. Zhu, Z. Luo, H. Chen, Y. Dong, S.-T. Wu, *Opt. Express* **2015**, *23*, 23680.
[37] W. L. Bond, *J. Appl. Phys.* **1965**, *36*, 1674.
[38] J. Xu, L. Wang, X. Zhao, Y. Shi, Y. Shi, T. Liu, *Nanomaterials* **2021**, *11*, 959.